UC Davis
UC Davis Previously Published Works

Title
Quantifying organic solar cell morphology: A computational study of three-dimensional maps

Permalink
https://escholarship.org/uc/item/5b11p2bf

Journal
Energy and Environmental Science, 6(10)

ISSN
1754-5692

Authors
Wodo, O
Roehling, JD
Moulé, AJ
et al.

Publication Date
2013-10-01

DOI
10.1039/c3ee41224e

Peer reviewed

PAPER

Quantifying organic solar cell morphology: a computational study of three-dimensional maps†

Olga Wodo,‡[a] John D. Roehling,‡[b] Adam J. Moulé*[b] and Baskar Ganapathysubramanian*[ac]

Establishing how fabrication conditions quantitatively affect the morphology of organic blends opens the possibility of rationally designing higher efficiency materials; yet such a relationship remains elusive. One of the major challenges stems from incomplete three-dimensional representations of morphology, which is due to the difficulties of performing accurate morphological measurements. Recently, three-dimensional measurements of mixed organic layers using electron tomography with high-angle annular dark-field scanning transmission electron microscopy (HAADF-STEM) provided maps of morphology with high resolution and detail. Using a simple, yet powerful, computational tool kit, these complex 3D datasets are converted into a set of physically meaningful morphology descriptors. These descriptors provide means for converting these large, complicated datasets ($\sim 5 \times 10^7$ voxels) into simple, descriptive parameters, enabling a quantitative comparison among morphologies fabricated under different conditions. A set of P3HT:endohedral fullerene bulk-heterojunctions, fabricated under conditions specifically chosen to yield a wide range of morphologies, are examined. The effects of processing conditions and electrode presence on interfacial area, domain size distribution, connectivity, and tortuosity of charge transport paths are herein determined directly from real-space data for the first time. Through this characterization, quantitative insights into the role of processing in morphology are provided, as well as a more complete picture of the consequences of a three-phase morphology. The analysis demonstrates a methodology which can enable a deeper understanding into morphology control.

Broader context

The morphology of organic solar cells is known to strongly affect the functional properties of a solar cell. "Good" morphologies result in much more efficient devices than "bad" morphologies. However, characterizing and quantifying the exact properties between a "good" morphology and a "bad" morphology have been limited by the difficulty in measuring the morphology of all the components accurately. However, recent development of an electron tomographic method which can measure the morphology of all the components has enabled the quantification of morphology. Here, the measured morphology is quantified in different ways in order to break down the complicated 3D morphology into easily understood and manageable pieces of information. Effects of different processing conditions on the morphology and the implications that they have on device functionality are explored and discussed. This is one of the many steps toward understanding what a "good" or a "bad" morphology actually is and ultimately being able to design processing methods which can achieve the most desirable morphology.

1 Introduction

The field of organic photovoltaics (OPV) has experienced rapid improvement in device performance. These improvements have largely been a result of growing understanding into morphology's role in device performance as well as the synthesis of new materials.[1–8] Researchers have recognized that morphology affects a number of physical properties of the device, such as charge separation efficiency, charge mobility and recombination characteristics.[9–14] Moreover, it has been recognized that processing parameters, as well as the component materials, affect the morphology and thus the performance.[15–17] Developing a quantitative correlation among fabrication, morphology and performance characteristics would allow for the direct design of higher efficiency devices. Process control has suffered, however, from two challenges: incomplete three-dimensional representations of morphology and, subsequently, limited quantification and identification of advantageous or undesirable morphological features.

Currently, many models and descriptions of morphology exist. Six of the most cited works in the field of OPV involve

[a]*Department of Mechanical Engineering, Iowa State University, Ames, IA, USA. E-mail: baskarg@iastate.edu*

[b]*Chemical Engineering and Materials Science, University of California, Davis, Davis, CA, USA. E-mail: amoule@ucdavis.edu*

[c]*Electrical and Computer Engineering, Iowa State University, Ames, IA, USA*

† Electronic supplementary information (ESI) available: Details of the graph-based method. See DOI: 10.1039/c3ee41224e

‡ These authors contributed equally.

3060 | *Energy Environ. Sci.*, 2013, **6**, 3060–3070

This journal is © The Royal Society of Chemistry 2013

some attempt to relate morphology to device performance.[2,6,18-21] These articles made large contributions to the understanding of the role of morphology and its link to fabrication conditions. But the morphology measurements made in these articles, or the assumptions of the morphology present, do not contain a fully complete picture. This is largely due to the lack of a technique capable of accounting for all aspects of OPV morphology.

The most powerful technique to visualize the internal structure of organic blends to date is electron tomography (ET). This technique is used to reconstruct three-dimensional information based on a series of two-dimensional transmission electron microscope (TEM) images acquired for different orientations of the sample.[22] The most common TEM technique relies on bright-field (BF) phase contrast to resolve the different features present in the sample. This technique allowed for the first three-dimensional images of a series of organic solar cell blends.[23-26] An alternative TEM technique, energy filtered TEM (EFTEM), has been used recently to increase the contrast between the components[22,27] revealing a slightly more accurate picture of the morphology. However, the data available from these studies still only contain a limited picture of morphology, as the techniques are only strongly sensitive to one phase within the mixture. It has been shown that morphology may consist of multiple phases. For example, in the most studied system, *i.e.* poly(3-hexylthiophene):phenyl-C_{61}-butyric acid methyl ester (P3HT:PCBM), three phases have been recognized[28] and confirmed by other studies.[15,28-36] These consist of a pure, mostly crystalline P3HT phase (also referred to as "aggregated"), a mixed amorphous P3HT:fullerene phase, and a fullerene-rich phase.

Recent advances in tomography techniques, however, have now made it possible to map the three-phase three-dimensional morphology using a combination of high-angle annular dark-field scanning TEM (HAADF-STEM) and a contrast enhancing fullerene.[37] With the high signal-to-noise ratio and a physically relevant reconstruction model used in this technique, more accurate morphological information is obtained. Full details of the method are described in ref. 37, but a brief description is included in the ESI.† The previous inability to accurately represent morphology limited quantification to averaged quantities like domain size[38,39] or was based on incomplete binary maps of the active layer, as in our previous work.[40,41] But by quantifying these directly measured three-phase morphology maps, not only can the effects of three-phases be determined, but features which lead to high performance devices can be extracted, leading to a much more complete understanding of morphology. It is also possible to quantitatively determine how sensitive morphology is to varying fabrication conditions and differing component ratios, eventually leading to more precise morphology control.

In this paper, we build on our previous work by analyzing these very complex and convoluted datasets, decomposing them into a set of physically meaningful morphology descriptors[40] by extending our computational framework to account for a three-phase morphology. Specifically, the connectivity of the domains, the distance between domains and electrodes, the domain size distribution, and the tortuosity of charge transport paths are

quantified – all in the true three-phase, three-dimensional nature of the morphology. This framework has allowed us to precisely quantify the more-complete morphology's evolution with changing processing conditions for the first time.

Based on the analysis of the five films, the following major observations were made regarding the morphology's contribution to relevant device processes. When annealed, regardless of the annealing method, BHJ films contain comparable amounts of each phase formed; different processing conditions only change the amounts to a small degree. All of the films measured allow for efficient exciton dissociation, as the distances between material interfaces are small. Interfacial area between the phases is well balanced, possibly explaining the reason for optimal performance at a certain weight ratio. Annealing with a metal cap present forms a morphology with more straight rising charge-transport paths in the fullerene-rich phase, while unconstrained conditions allow P3HT domains to form more straight rising paths. Meanwhile, solvent annealing seems to provide the best conditions to develop balanced paths in terms of the overall tortuosity of charge transport paths. Finally, regardless of processing conditions or blend ratios, phases are well connected to the respective electrodes with a minimal fraction of islands.

2 Results and discussion

A series of thin films fabricated under five fabrication conditions were quantified, and each condition was specifically chosen to represent a morphology which has been well-studied in the OPV field. The films were comprised of a blend of P3HT:$Lu_3N@C_{80}$-PCBEH (EH, ethyl-hexyl). Four films were prepared with a weight ratio of 10 : 13, and one was prepared using 10 : 19 to increase the fullerene-rich phase content. Morphology data were measured by acquiring a tilt-series using HAADF-STEM and reconstructing the datasets using a discrete algebraic reconstruction technique (DART).[42-44] The reconstruction method has been demonstrated to give an accurate map of the materials within a bulk heterojunction (BHJ), and the endohedral fullerene serves as a suitable analog for PCBM, although it is slightly more miscible with P3HT (the mixed phase contains 30% by volume fullerene *vs.* PCBM's 20–35%).[33,45] Full details on the imaging and reconstruction methods are published elsewhere.[37] The preparation conditions and the sample names which are used hereafter in the text are given in Table 1.

Table 1 Samples used in the study. Given are the sample names used in the text, prepared weight ratios (P3HT:fullerene), the treatment done and the top electrode present during annealing (cathode, which was removed for ET measurements). For exact annealing conditions, see the Experimental section

Sample name	Weight ratio	Treatment	Annealed with Cap?
As-cast	10 : 13	None	No
SA	10 : 13	Solvent annealed	No
TA	10 : 13	Thermally annealed	No
CaCap	10 : 13	Thermally annealed	Ca (40 nm)
CaCap10 : 19	10 : 19	Thermally annealed	Ca (40 nm)

This journal is © The Royal Society of Chemistry 2013

Energy Environ. Sci., 2013, **6**, 3060–3070 | **3061**

These datasets are herein analyzed using a graph-based method. In our method, we construct a graph based on three-dimensional voxel-wise data. Due to such a representation, we gain the ability to use standard and efficient algorithms from the graph theory[40,41] to extensively characterize morphology. In particular, we use two fundamental morphology characteristics – connectivity and path length – and convert them into graph features. These features are important from an OPV point of view, and at the same time standard and well-studied algorithms are available for graphs. The graphs have two main components: (i) vertices corresponding to voxels with labels denoting the phase, and (ii) edges encoding local neighborhood of the vertices. We use first- and second-order neighbors to construct edges. Thus, six 'geographically' nearest neighbors (horizontal and vertical) as well as 20 second order neighbors (diagonal) are considered.§

Using the density of each component, the volume percent of each component in the 10 : 13 films was calculated to be ~60% P3HT and ~40% fullerene, nearly equivalent to that of a 1 : 1 by weight P3HT:PCBM mixture. The 10 : 19 films were calculated to be ~50% P3HT and ~50% fullerene. Densities were taken to be 1.10 g cm^{-3} and 2.07 g cm^{-3} for P3HT and Lu$_3$N@C$_{80}$-PCBEH, respectively.[45,46] This set of samples gives a wide variety of morphology conditions to characterize and compare.

An important point in this characterization is how the metal capped films were prepared. It is an often practiced procedure that the morphology of a layer is characterized after the film is annealed without a metal cap present. However, most devices are annealed *with a metal cap present*, and that has been shown to drastically affect the material's distribution within the layer.[47] Here, two cases are examined, where the film was annealed without a capping metal present (TA and SA) and annealed with a capping metal present (CaCap and CaCap10 : 19). The change in morphology that occurs with annealing with a metal cap has a significant effect on the PCE of a OPV device.[6] These are important points to consider when fabricating devices, as the sample history has an effect on the morphology.

Three phases were determined to be present within each of the five analyzed films: a pure P3HT phase, a fullerene-rich phase and a mixed phase of polymer and fullerene (referred hereto as "mixed"). The abbreviations "D", "M", and "A" refer to the electron donor (P3HT), mixed, and electron acceptor (fullerene) phases, respectively. All datasets have a voxel unit length of 1.4 nm.

The DART algorithm is able to reconstruct morphology accurately by using discrete gray levels to represent different materials in the reconstruction process. This is a physically relevant representation assuming that the imaged materials contain a consistent composition and density (which is a

§ Considering second-order neighbors ensures that shortest paths are computed based on diagonal, horizontal, and vertical paths. Path lengths are particularly sensitive to the choice of neighborhood, especially for highly torturous paths. Full details on the graph-based method and various morphology descriptors are published elsewhere.[40,41] For completeness, details of the graph constructions as well as basic algorithms are given in the ESI. In the result section, we seek to emphasize the link between these morphology descriptors and the fabrication process. We very briefly allude to how these physics-based morphology descriptors may be correlated with the subprocesses of photovoltaic operation.
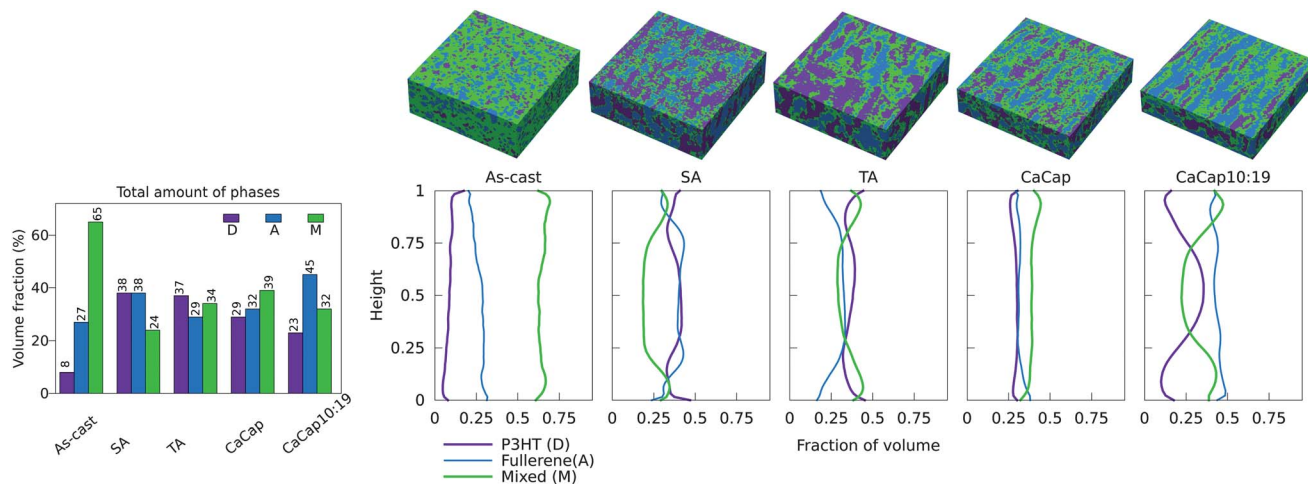
reasonable assumption for these materials at the resolution used). The reconstruction process consists of finding the right number and value of gray levels which results in a reconstruction where the forward-projection matches the original tilt-series as closely as possible (minimizes the difference between the forward-projected reconstruction and the original tilt-series). For the films used in this study, it was found that three gray levels were necessary for the best fit to the data. The thresholds and gray levels were manipulated until the best possible fit to the data was found (minimized residuals). No subjective segmentation is necessary, thus ensuring that the reconstructed morphology is not dependent on an assumed threshold. Previous attempts to quantify morphology through manual thresholding resulted in large uncertainties in the quantification. This occurred because the segmented reconstructions were not constrained to match the original images and therefore finding the "right" threshold is subjective.[48] Here that problem is avoided because the segmented reconstructions match the original data.

Because of the large number of voxels in each dataset (~5 × 10^7 voxels), each dataset was divided into representative volume elements (RVEs),[49] as required by the computational framework's memory. Each RVE consists of all voxels along the film's height (thickness) and 200 × 200 voxels in the remaining dimensions. Additionally, a plane of pixels on the top and bottom of the datasets was cropped out of the analysis due to a reconstruction artifact which results in more P3HT phase being artificially mapped in these planes. The size of the RVE was increased and all metrics were recalculated until the edge-effects were minimized and the statistics (across all the RVSs associated with a sample) had converged. For all five films, we computed the standard deviation over all RVEs for each morphology descriptor. For each film, the standard deviation of morphology descriptors across RVEs was smaller than 5% (less than 1% for most cases), demonstrating that the films were relatively homogeneous. This small variation of individual morphology descriptors ensures that the RVE size is appropriate, and that RVEs are in fact representative of the entire film. Furthermore, we tested both periodic and non-periodic boundary conditions and found very consistent results. This ensures that end-effects are not significant. This is important because it also suggests that the morphology data, which are only about 1.5 μm^2 in the measured area, are representative of the entire film's morphology.

The RVEs were then quantified identically and an extended list of morphology descriptors was constructed along with characteristic histograms. Subsequently, average morphology descriptors were computed for each RVE. All quantities included in this manuscript are averaged over all RVEs in a given film. However, histograms are constructed for the most representative RVE. The most representative RVE is chosen such that its vertical material profile most closely resembled that of the entire sample.

2.1 Describing morphology

Fig. 1 shows each film's most representative RVE, the volume of each phase comprising the films, and the vertical volume

Fig. 1 (Top) Solid rendering of a representative section (RVE) of each film measured. (Bottom) Total amount of each phase present in each film and vertical segregation profiles for all five films. In the plots, zero corresponds to the cathode side and one corresponds to the anode side (substrate).

fraction of each phase through the film's thickness. A few immediate trends are noticeable. First, the annealed films (SA, TA, CaCap) all have comparable volume composition of the three phases, roughly a third for each phase, which is much different from the As-cast film, even though all four films were fabricated with the same blend ratio (10 : 13 by weight). When the films are allowed to relax (by undergoing an annealing process), a comparable amount of each phase forms, regardless of the processing conditions. This may indicate a preferred configuration for this system, with the partial miscibility and self-aggregation of the components driving this apparent ratio. It must be noted that the volume percent of fullerene in the mixed phase was calculated to be ∼30% for all films, except the TA (49%).

The vertical distribution of materials in the films is dependent on processing.[46,47] Two films, the As-cast and the CaCap, do not show large changes in composition throughout the thickness. However, three other films, SA, TA and CaCap10 : 19, reveal very pronounced changes as well as similar shapes of vertical composition, namely double well profiles in the P3HT phase. The links between fabrication and vertical segregation have been discussed in another publication in more detail,[47] but the vertical profile does have an effect on the morphology descriptors, and will be discussed later in section 2.4.

Fig. 2 illustrates the relative interfacial area between individual phases, D–M, D–A and A–M. Regardless of processing, all films show very similar interface composition characteristics. For all films, the interface between D and A is almost nonexistent (less than 2% of the total interface). The lack of a D–A interface quantitatively confirms that the mixed phase is distributed between the D and the A phases. Consequently, the interfaces between the mixed phase and the two pure phases represent most of the interfacial surface area in all films. For the annealed films with the same blend ratio, the D–M and A–M interfaces constitute a comparable fraction of the total interface, which is close to 50%. The film with increased fullerene (CaCap10 : 19) has more A–M interface (60%) than the D–M
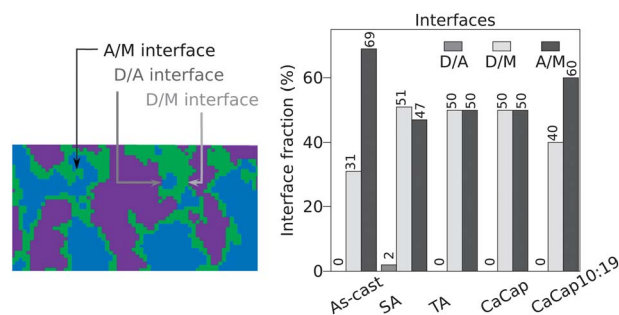

Fig. 2 Breakdown of the relative interfacial surface area between the different phases. Given are the P3HT–mixed interface (D–M), P3HT–fullerene-rich interface (D–A), and fullerene-rich–mixed interface (A–M). There is virtually no D–A interface in any of the films studied.

(40%) interface, which is not surprising as there is more fullerene present in the film.

The balanced interfacial area between the D–M and A–M interfaces is likely a result of the volume fraction balance in material phases as seen from Fig. 1. The balance in interfacial
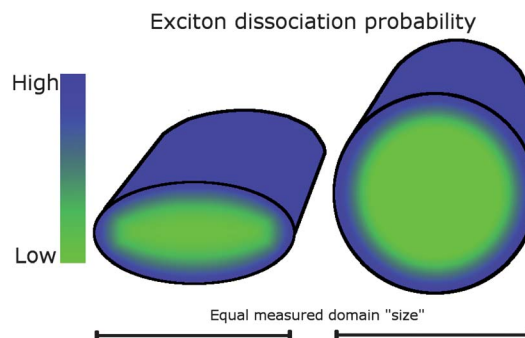

Fig. 3 Diagram demonstrating the probability of an exciton generated within a domain to reach an interface between phases for two different cross-sectional shapes. Note that an elliptical cross-section has a higher average probability for an exciton to reach an interface, despite the same measured domain "size" (width).

This journal is © The Royal Society of Chemistry 2013

Energy Environ. Sci., 2013, **6**, 3060–3070 | **3063**

area between A–M and D–M interfaces may be one reason why a 1 : 1 by weight P3HT:PCBM mixture outperforms other mixing ratios.[1,2,10] The 10 : 13 and 10 : 19 P3HT:Lu$_3$N-PC$_{80}$BEH films have the similar component volume ratios as 1 : 1 and 2 : 3 P3HT:PCBM films, respectively. We assume that the morphology of Lu$_3$N-PC$_{80}$BEH and PC$_{60}$BM films are similar because of very similar measured domain sizes[23] and miscibilities of the two mixtures.[33,45]

The comparison between films containing different fullerenes is difficult however, and only estimations can be made. It must be noted that the optimum blend ratio for the best device performance from a similar endohedral fullerene (substituting a hexyl group for the ethyl-hexyl group on the ester), was found by Ross *et al.* to be 1 : 1 by weight.[50] This means that the optimized device using a slightly less miscible fullerene (because of the different side group[37]) contained a larger total P3HT volume compared to the films studied here. We therefore consider our results consistent with all published results on endohedral fullerenes. On a side note, these results have led us to believe that, through control of the side chain length, endohedral fullerenes can be adjusted to fit the miscibility of various reported fullerenes.

Another notable trend is the amount of pure, aggregated P3HT present in the annealed films. By examining the ratio of the P3HT phase's volume to the total expected P3HT volume (~60% for the 10 : 13 films), the amount of P3HT aggregation can be calculated. The crystallinity of the pure P3HT phase cannot be determined with this measurement technique, however, we confirm that it does not contain fullerene, therefore can be considered as pure. We make this distinction because measuring the overall crystallinity of a BHJ mixture has proven to be very difficult[22] and the packing of polymer domains can be very indefinite, as other studies have shown.[51,52]

The TA and SA films are observed to have 62% and 63% aggregated P3HT, respectively, while both the Ca capped films only have ~50%. It seems as if heating with a metal present causes reduced P3HT aggregation.[47] The phase profiles also show a decrease in aggregated P3HT nearby the interfaces in the annealed films, and an increase in the mixed phase (which contains amorphous P3HT). The recovery of aggregated P3HT directly adjacent to the interfaces is difficult to determine whether it occurs from a reconstruction artifact or from accurate measurement. However, the decrease in P3HT aggregation just below the surfaces is measured accurately and has implications on device function. Because of the increased mixed phase near an electrode, charges may have to pass through the mixed phase to get to the electrode. This may increase the trapping of charges in these disordered regions and also increase recombination.[13,53] Therefore, finding a way to mitigate the increase in the mixed phase nearby the electrodes may help increase solar cell efficiency.

2.2 Quantifying morphology with exciton diffusion

In order to quantify morphology with respect to exciton dissociation, path lengths from potential locations of electron excitation to the interface (where charge separation is energetically favorable) were quantified. Distances are of particular interest because an exciton has a very short lifetime, during which it
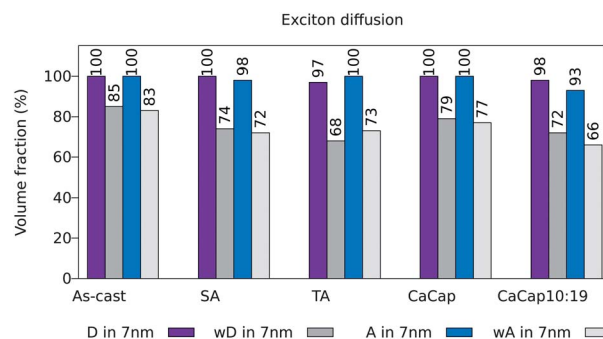

Fig. 4 Fraction of D and A within an exciton diffusion length of the interface, taken to be 7 nm. Weighted volume fraction of D and A (wD and wA), where each pixel is weighted based on the distance from the interface ($\exp(-d/L_d)$), illustrated visually in Fig. 3.

travels diffusively, and the exciton is considered useful only when it reaches an interface and dissociates. For each voxel we find the shortest distance to the nearest interface and use it as a local characteristic length for diffusive transport. We then weight the contribution of this voxel to exciton diffusion/dissociation by the function ($f = \exp(-d/L_d)$). This exponential distribution encodes the chance of an exciton traveling a certain distance d and finding the nearest interface. The parameter representing this distribution is the exciton diffusion length, L_d. If the distance to the nearest interface is much longer than L_d, the exciton—with high probability—will return to a ground state before reaching the interface. On the other hand, excitons generated near an interface have a high probability to reach the interface. Finding shortest distances as well as weighting are done for each voxel of interest in the morphology. Finally, to assess the morphology-scale feature with respect to exciton diffusion we average weighted distances for all voxels of interest: $wf = \sum_{i}^{n_D} w(d_i)/n_D$, where n_D is total number of D voxels (or A voxels if the acceptor absorbs light efficiently). In the ESI,† we include examples to illustrate this descriptor in more details.

In contrast to this descriptor, other approaches compare the average domain size[38,39] to the exciton diffusion length, L_d. These provide a coarse morphology quantification with respect to exciton diffusion whereas the descriptor proposed here encodes the local topology of the morphology. We note, however, that our approach, although more detailed than other descriptors commonly used, does not account for all aspects of the exciton transport process. In particular, we choose only one characteristic distance (the shortest distance to the interface), while an exciton may not necessarily find the closest segment of the interface during a random walk.¶ This descriptor however shows a high correlation with a more complex descriptor accounting for a more detailed random walk dynamics as well as a full scale analysis, as outlined in the ESI.†

¶ One of the reviewers suggested using a more detailed descriptor that represents the random walk dynamics more accurately. We show in the ESI that this more complex descriptor gives results nearly equivalent to the simpler descriptor used here. The key motivation for using the simpler descriptor is the substantial increase in computational complexity involved with the more complex descriptor.

3064 | *Energy Environ. Sci.*, 2013, **6**, 3060–3070

This journal is © The Royal Society of Chemistry 2013

Fig. 4 shows the fraction of the P3HT and fullerene-rich phases which are within an exciton diffusion length ($L_d = 7$ nm) of an interface. It can be seen that nearly all of both the P3HT and fullerene-rich phases are within 7 nm of an interface, more than 97% of the P3HT and at least 93% of the fullerene-rich phase. There are differences of only a few percentage points using this analysis. But the probability of an exciton reaching a donor–acceptor interface is also shown in Fig. 4 (grey boxes); here the differences between films are much more pronounced. It is clear that nearly three quarters of both phases in all five films show very good characteristics with respect to exciton diffusion, but the CaCap and As-cast seem to have the best morphology for efficient exciton dissociation.

To differentiate further between the films, histograms plotting the phase-fractions distributed within a given distance of the interface are shown in Fig. 5, along with the average value of these distances. In the As-cast film, nearly all of the P3HT phase is distributed within two voxels from the interface (see the histogram with box size corresponding to the voxel unit length), with as much as 70% of the total P3HT phase directly adjacent to the interface. This is in line with volume fraction occupied by P3HT in the As-cast film, which is only 8% of the total sample. Since domains are small, the average distance to the interface is also small, in this case 1.16 nm. All of the annealed films have similar histogram profiles, except for the CaCap, which has a smaller average distance to an interface. Greater than 40% of both phases are located within a single voxel of the interface in this film. Of all the annealed films, it shows the best morphology characteristics with respect to exciton diffusion. It is also likely that the mixed phase would separate excitons efficiently because of the close physical proximity of both components. Accounting for this, the As-cast film still shows the best morphology characteristics for exciton dissociation, as it has the smallest average distance and the largest mixed phase fraction, followed by the CaCap film.

It may be surprising that there are measurable differences between the annealed films because the average domain size of the P3HT is similar, about 15–20 nm. However, the measurements presented here hint that the relevant characteristic length needed for efficient exciton dissociation is not the measured width of a domain. If one considers a single domain, with a circular cross-section, the average shortest distance from the interior of the domain to the outside is calculated to be one-sixth of the diameter, or one-sixth of the measured domain size ($\int_0^R r(R - r)dr / \int_0^R r dr = R/3$). This corresponds to 2.5–3.5 nm in a 15–20 nm diameter domain. But domains can have different shapes; in the annealed films the average distance to an interface in the P3HT is <2.5 nm. This suggests that the domains are not circular in cross-section, but are closer to elliptical. This was indeed confirmed by examining the reconstructions visually. Therefore, the domain size is clearly not the best measuring stick for efficient exciton dissociation, as it does not measure the average distance excitons travel before they are dissociated or recombine. Fig. 3 illustrates this point of how different domains, with the same measured domain size (width), can have different average distances to an interface.

2.3 Connectivity of domains to relevant electrodes and tortuosity of paths

The connectivity of the P3HT and fullerene-rich phases to their relevant electrodes is very important for organic blends to function well as a photovoltaic device. Only the domains which are directly connected to the electrodes can constitute "pathways" for charges to travel from interfaces (where charges are separated) to electrodes.

Table 2 shows the connectivity of P3HT domains to the anode, the fullerene-rich phase to the cathode, and of the mixed phase to both electrodes. For the P3HT phase, all the annealed films have very high connectivity. More than 96% of the volume of P3HT is connected to the anode for all of the annealed films. The As-cast film shows only 30% connectivity, but this is due to low volume fraction of the phase, *i.e.* 8% which is much below the percolation threshold for 3D morphologies ($\sim$30%).[54] For
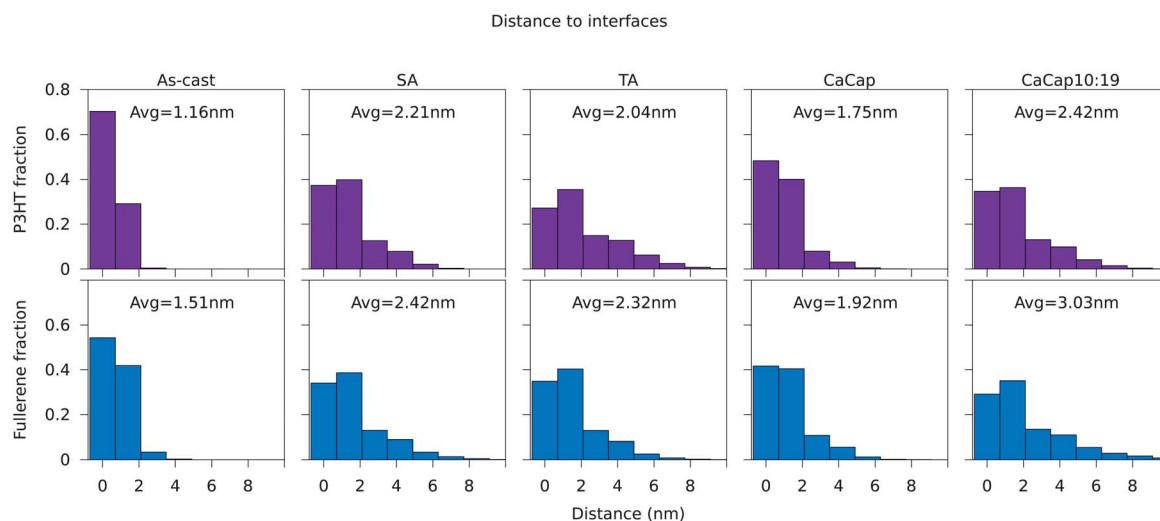
Distance to interfaces

Fig. 5 Detailing of the distances to the interfaces; shown are the fraction of P3HT within a certain distance to the D–M interface (top) and the fraction of the fullerene-rich phase within a distance to the A–M interface (bottom).

This journal is © The Royal Society of Chemistry 2013

Energy Environ. Sci., 2013, **6**, 3060–3070 | **3065**

Table 2 Volume fraction of phases connected to their respective electrodes

Sample	P3HT connected to anode	Mixed connected to anode and cathode	Fullerene connected to cathode
As-cast	29.8%	100%	94%
SA	99.6%	99.8%	99.5%
TA	99.4%	99.9%	98.3%
CaCap	99.3%	99.9%	99.4%
CaCap10 : 19	96.8%	99.8%	99.8%

the fullerene-rich phase, all films, even the As-cast sample, have a connectivity larger than 94%. The mixed phase, because of its location directly between the other phases, has a very high connectivity to both electrodes. Our analysis quantitatively shows that phase connectivity to electrodes is insensitive to processing, and all annealed films have high connectivity with a very small fraction of island formation. This surprising result is very important for device performance. Effectively, the entire volume of the device contributes to charge transport, regardless of processing conditions. Furthermore, this high bulk connectivity of all three phases explains the observation by Wang et al.[55] regarding the contact area with the electrode. They speculated that as long as the contact area between fullerene and cathode is nonzero (even as low as 3%), it enables electron extraction. Our results provide an explanation for this behavior. All phases have high volumetric connectivity within the bulk of the active layer. Therefore, as long as the contact with electrode is nonzero, the bulk is also highly connected to the electrode.

High connectivity is, however, a preliminary condition for good charge transport and does not take into account the path length that charges must traverse to reach the electrodes. In particular, the larger the distance the charge needs to travel to reach the electrode, the higher the probability of recombination. Moreover, the more tortuous the path is, the higher is the probability of encountering the interface with another phase and subsequent recombination. Tortuosity is defined as a ratio of the straightest path through the morphology (assuming that paths can consist of only one type of phase) to an actual straight path (the shortest possible path). For such a definition, paths with tortuosity equal to one have an actual path which is the shortest possible.

These paths are considered straight rising paths. The shortest path for every *connected* voxel (only those which are connected to the electrode) of the charge transporting phases to their respective electrode, P3HT to the anode and fullerene-rich to the cathode, respectively, was computed for all films.

Fig. 6 illustrates the different pathways that a charge can take, illustrating the tortuous nature of the domains. The two-dimensional representation is insufficient to show the three-dimensional nature of the charge transport but readily demonstrates the different processes charges undergo. The three-dimensional representation illustrates the 3D nature, but is difficult to visualize. This demonstrates the complicated nature of these datasets and the power the morphology descriptors have to simplify them into easily understood parameters.

The volume of each phase which has straight rising paths to the electrodes is shown in Fig. 7. Clearly, very little of any film is capable of charge transport without undertaking a curved path or the charges having to move through a different phase.

To gain further insight into the tortuosity, tortuosity distribution histograms were calculated, which are shown in Fig. 8.
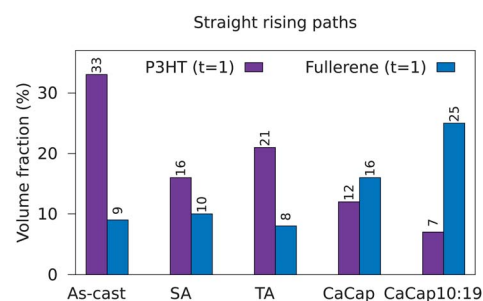
Fig. 7 Percentage of electrode-connected P3HT and fullerene-rich phase pixels with straight-rising paths (tortuosity = 1). This illustrates the low probability of most charges being able to move in a straight line to an electrode.
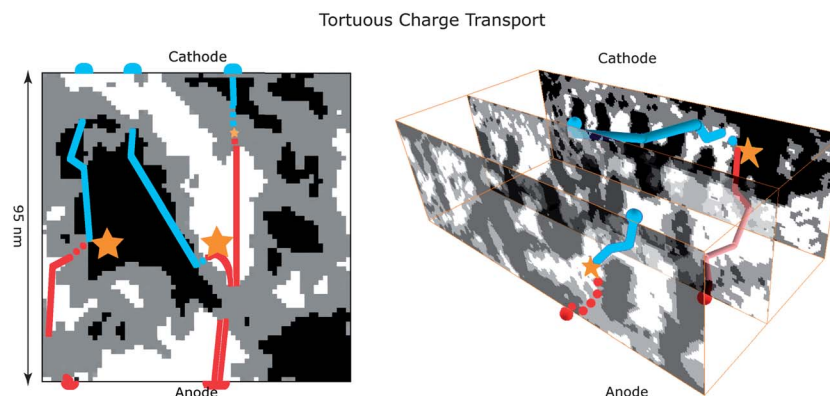
Fig. 6 A small slice (left) and volume (right) of the TA morphology map and illustration showing exciton dissociation and charge transport in a BHJ film. Phase colors are omitted for clarity: P3HT (black), mixed (gray), and fullerene (white). Stars represent dissociating excitons. Generated charges must then traverse the mixed phase (dots) to the component phases (P3HT or fullerene-rich). Once within the component phases, the charges may not be able to travel in straight lines, but must use tortuous pathways to the electrodes (red and blue lines are holes and electrons, respectively).
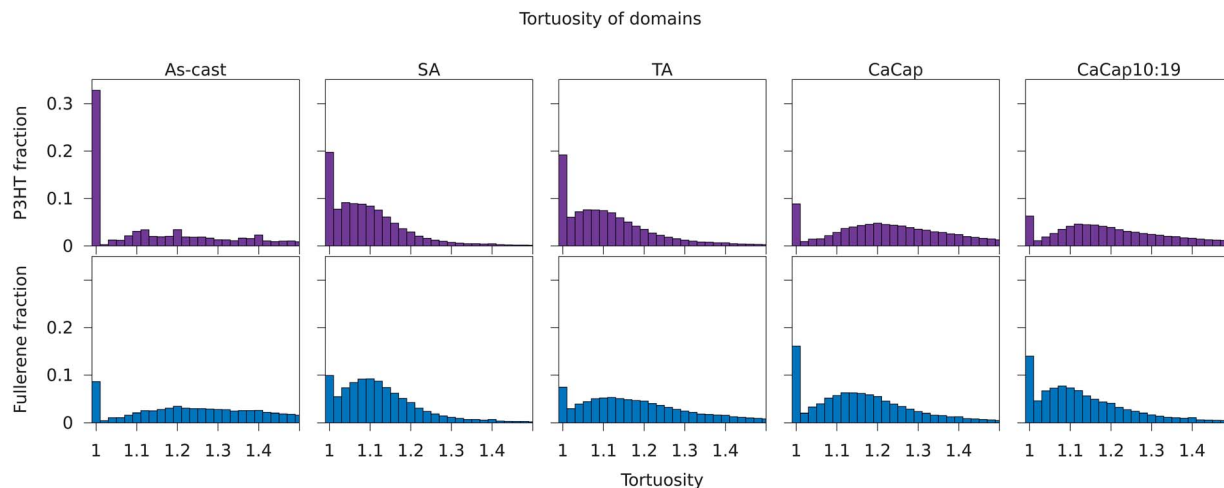
3066 | *Energy Environ. Sci.*, 2013, **6**, 3060–3070

This journal is © The Royal Society of Chemistry 2013

Fig. 8 Histogram of tortuosity of P3HT and fullerene-rich phases' paths to their respective electrodes. These display the distribution of tortuous paths through each sample, differentiating between films with similar fractions of winding paths.

The P3HT domains of the annealed films show that the uncapped films (SA and TA) have distributions similar to each other, as do the capped films (CaCap and CaCap10 : 19). Although the capped films have paths with higher tortuosity and a wider tortuosity distribution, for the fullerene-rich domains, the opposite trend is true for P3HT domains. The capped films result in less tortuous paths, while the uncapped films have more tortuous pathways. Capping the films with a metal clearly must have an effect on the distribution of domains and thus, the tortuosity. It has been shown that including the capping metal during heating results in more fullerene moving to the interfaces, which is likely why the tortuosity decreases for a fullerene-rich phase.[46,47] Interestingly, this increases for the P3HT phase. With both fullerene and P3HT crystallization driving the morphology formation,[37,56] the movement of the fullerene to the top and bottom of the film must cause the P3HT to be more tortuous. It seems that the interplay between the three phases has a large effect on the formation of the morphology and annealing while the film is capped changes this interplay. It must be noted that the calculations of tortuosity were the most sensitive quantities with the highest standard deviation between RVEs. Variations between different RVEs could affect these calculations to some degree, but do not affect our overall conclusions.

For a device to function well, the mobilities of both phases must be equalized.[57] One can imagine, however, that an imbalance in path-lengths would lead to a similar effect. This is because only when two types of charges are collected at respective electrodes, are charges considered useful. Therefore, the balance of the different charge paths is another important aspect of device function. The balance can be defined in different ways. For example, it can be assessed solely based on distances, tortuosity or the mobility of charges. Here, we consider the balance of tortuosity between the P3HT and fullerene-rich phases' path-lengths.

Fig. 9 depicts the balance of charge pathways for all films. In this figure, spline-fitted histograms of tortuosities from Fig. 8 are overlaid for each film. However, here fractions are computed with respect to the volume of the film, which compares the total amount of the material with a particular tortuosity. This analysis allows direct comparison of all the films. In particular, we compare different configurations – with and without metal capping, to assess path balance. Such a comparison gives insight into the effect of capping.

When both curves overlap, e.g. the SA film, paths of both types are balanced. It means that in such a film, there are comparable numbers of paths with the same tortuosity. When there is minimal overlap between areas under both curves, the film has
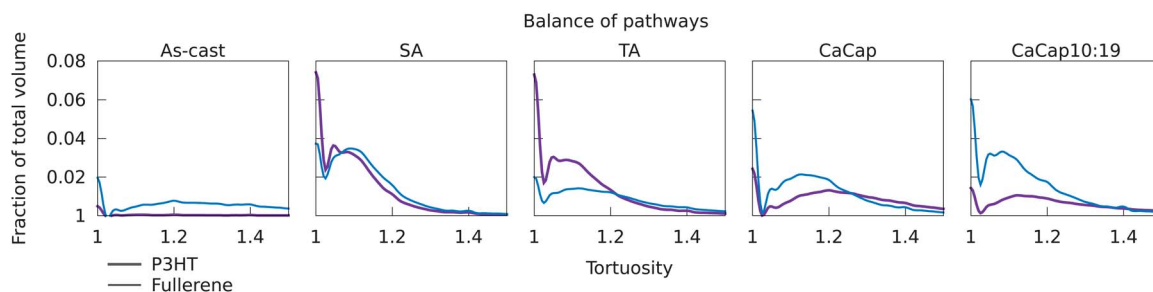

Fig. 9 Balance of path tortuosities: an overlaid spline-fitted histogram of path tortuosities (from Fig. 8). Fractions are computed with respect to volume of the film allowing assessment of the fraction of the film with complementary path characteristics. When both curves overlap, e.g. SA film, paths of both types are well balanced, i.e. there are comparable number of paths with the same tortuosity.

This journal is © The Royal Society of Chemistry 2013

Energy Environ. Sci., 2013, **6**, 3060–3070 | **3067**

highly unbalanced characteristics, *e.g.* the As-cast film, where volume fraction of P3HT is much lower than those of fullerene-rich domains. Path balance can be considered a higher order morphology descriptor, because it can be affected by unbalanced volume fractions of considered phases, or by vertical segregation. Nevertheless, path balance is a useful approach to assess the charge transport propensity of the analyzed films.

Our analysis indicates the SA film as possessing the best tortuosity balance, followed by the Ca capped 10 : 13 film, the TA film, the Ca capped 10 : 19 film and finally, the As-cast film. Experimental evidence suggests that SA films indeed possess a higher balance of paths than TA films because the filling factor (FF) and short-circuit current (J_{SC}) are higher than those of a TA device.[58] An imbalance of paths would likely cause this. In an imbalanced film, the photocurrent would be reduced by the longer path-length of one of the charges, which would cause a space-charge build up, thereby decreasing the FF and J_{SC}, as seen in the TA film.[57]

Additional experimental evidence of possible path-length imbalances has been shown in mobility measurements made of BHJs. Studies found that the fullerene phase had an order of magnitude higher mobility than the P3HT.[14] Since the measurements were made on an actual BHJ, it is likely that these mobilities were influenced by the path balance as well as by the intrinsic mobilities of the materials; however, it is difficult to assign which would have the dominating effect.

This has strong implications for device function. If we assume that the mobility which was measured was indeed the intrinsic mobility, then a more tortuous fullerene-rich phase would result in better balance of charge-transport. Since its mobility is higher, longer paths for electrons are needed. In this case, the uncapped films would perform better. However, if the fullerene had a lower intrinsic mobility than the P3HT, then a more tortuous P3HT phase would perform better, and metal capping would be the better fabrication condition.

Connectivity, path balance and tortuosity of paths are insightful physics-based morphology descriptors. However, they do not cover all aspects of the morphology in the context of charge transport. In particular, anisotropy of charge transport along and across polymer chains are of particular interest in elucidating charge transport. The imaging technique used here precludes this quantification. Ideally, additional data that resolve degree of crystallinity or positions of individual atoms (*e.g.* molecular dynamic simulations) would be required to quantify paths in more detail. Given more resolved data, the graph-based technique used can be easily extended to these descriptors.[40]

2.4 Mixed phase

The last set of morphological descriptors analyzed examines the mixed phase. The mixed phase is the least quantified in terms of topological properties, mostly because only recently it has been recognized as a separate phase observed in certain classes of organic blends.[15,22,28] As determined before, the mixed phase is distributed between two main phases. The mixed phase likely serves as the interface where charge dissociation and bimolecular recombination occur, as it is nearly the only place where the
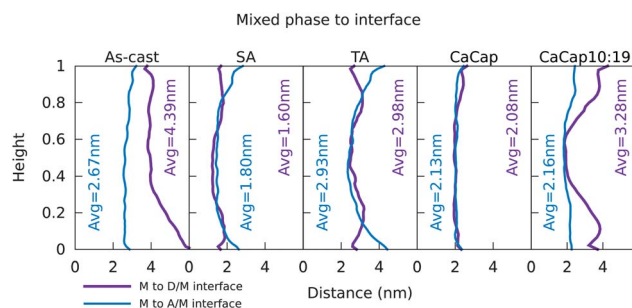

Fig. 10 Vertical distribution of distances from the mixed phase to the D–M (light) and A–M (dark) interfaces. The averages over the entire film are given in each plot as well.

different components are physically adjacent to one another. Once excitons separate, the charges must travel within the mixed phase to the component phases (as shown in Fig. 6). Therefore, transport properties of paths within the mixed phase towards other phases are very important. In particular, they have implications on charge generation as well as recombination.

The distances from all mixed voxels to the D–M interface as well as from mixed voxels to the A–M interface were computed. This was done is an analogous way to calculations of distances from D to D–M interface discussed in section 2.2. The averaged distances in both directions are shown in Fig. 10. For all the films but the As-cast and the CaCap10 : 19, the average distances in both directions are comparable. However, in the As-cast and CaCap10 : 19 films, the average distances differ significantly (by a factor of 1.5). Explanation of the distance anisotropy is given in the ESI.†

The distances across the mixed phase are important. As illustrated in Fig. 6, after dissociation one charge type must traverse through the mixed phase in order to reach a pure phase, where it can then be transported more easily. The necessity to traverse the mixed phase occurs for both electrons at the D–M interface and holes at the A–M interface. A balance between these two path lengths is desired for balanced charge extraction rates. An imbalance of the path lengths in one direction would likely result in an imbalance of charge transport through the mixed phase and could lead to charge build-up and increased recombination. A local space-charge results in a lower efficiency device.[57] Since the mixed phase is nearly the only place where the components are in direct contact with one another, it is likely that most recombination happens at the mixed phase interfaces or within the mixed phase itself. Therefore, the balance of paths in the mixed phase is a very important parameter to control.

The mixed phase distances seem to follow the same trend as the vertical profile of the P3HT and fullerene-rich phases. This indicates that the local amount of these phases strongly affects the mixed phase distances. Therefore, the vertical profile, which is affected by processing conditions, is also important to be considered and controlled.

3 Conclusions

We quantitatively characterized the morphology of five polymer:fullerene blend films. Using two mixing ratios, and a spectrum of processing conditions, we effectively established a link between

3068 | *Energy Environ. Sci.*, 2013, **6**, 3060–3070

This journal is © The Royal Society of Chemistry 2013

processing and morphology. The effects of processing conditions on interfacial area, effective domain size distribution, and tortuosity of charge transport paths are determined. All of the above metrics are built based on OPV specific physics which decode morphological properties into meaningful parameters, which can then be compared between different processing conditions.

Based on the analysis of five films, the following observation was made. First, when the films are allowed to relax (by undergoing an annealing process), a comparable amount of three phases are formed. Additionally, an interface between the P3HT and fullerene-rich phases is nearly nonexistent in all five films, regardless of processing; this quantitatively confirms that the mixed phase is distributed between the P3HT and fullerene-rich phases. It was also found that the total interfacial area between the mixed–P3HT phases and the mixed–fullerene-rich phases are comparable for all annealed films of the same blend ratio. Each of the films has good morphological characteristics related to exciton diffusion in the P3HT and fullerene-rich phases, with a large fraction of both contributing to generation of separated charges. Among the annealed samples, the CaCap sample reveals the best morphological features related to exciton dissociation. It also seems that metal capping provides better conditions for fullerene-rich phases to develop more straight rising paths, while an unconstrained geometry allows P3HT domains to form more straight rising paths. Solvent annealing seems to provide the best conditions to develop balanced paths for both domains. Lastly, regardless of processing conditions and blend ratios, all of the phases are well connected to electrodes with a minimal fraction of islands formed, revealing the naturally forming interpenetrating morphology of this P3HT:fullerene blend.

From these analyses, we conclude that of the five films, the CaCap film seems to have the best morphological characteristics to provide high performance. It has the best balance of interfacial area, the best morphological features for exciton dissociation, as well as the best charge transport morphological characteristics through the mixed phase. Although the tortuosity balance in this film is not as favorable as that in the SA film, the other factors will likely outweigh this. This seems quite remarkable, as this morphology is what forms in an actual device structure.

These observations have continued to develop our knowledge of morphology and its link with processing and the properties of devices. The analysis introduced here also reveals a more complete picture of the consequences of a three-phase morphology, and increases our understanding of morphology control.

4 Experimental

4.1 Film preparation

Samples for TEM measurements were prepared by first cleaning glass substrates and spin-casting a 40 nm layer of poly (3,4-ethylenedioxythiophene):poly (styrenesulfonate) (PEDOT:PSS). They were then placed into a N_2 glovebox and a solution of P3HT:$Lu_3N@C_{80}$-PCBEH dissolved in chlorobenzene (~20 mg mL^{-1}) was spin cast onto the PEDOT:PSS. Film thicknesses ranged from 70 to 100 nm. The TA film was annealed at 150 °C for 5 minutes and the SA film was annealed in a 1,2 dichlorobenzene saturated environment at 150 °C for 2 hours; afterwards, the film was dried for several days in a vacuum. For these two films the top interface was N_2 during the annealing process. The CaCap and CaCap10 : 19 films were placed into an evaporation chamber and 40 nm of Ca was evaporated onto the films. They then were annealed at 150 °C for 5 minutes and the Ca was subsequently washed off with water (to accommodate HAADF-STEM imaging). All the films were then taken out of the glove box and floated off the glass substrates in water (due to the soluble PEDOT:PSS layer) and then picked up with lacey carbon TEM grids.

4.2 HAADF-STEM imaging and reconstructions

All imaging was performed on a JEOL 2100F microscope at 200 kV using DigitalMicrograph™ (Gatan) with a tomography plugin capable of dynamic focusing (keeping the film in focus when tilted). Images were taken at one degree intervals from a minimum of +65 to −65 degrees and aligned manually using IMOD. 3D reconstructions were done using a custom code in MATLAB implementing the DART algorithm. The reconstructions matched the original images as closely as possible while maintaining a realistic physical model (constant gray level for a single phase). More details of the reconstruction method can be found in ref. 37 and 42 and the ESI.†

References

1 D. Chirvase, J. Parisi, J. C. Hummelen and V. Dyakonov, *Nanotechnology*, 2004, **15**, 1317–1323.
2 G. Li, V. Shrotriya, J. Huang, Y. Yao, T. Moriarty, K. Emery and Y. Yang, *Nat. Mater.*, 2005, **4**, 864–868.
3 M. Reyes-Reyes, K. Kim and D. L. Carroll, *Appl. Phys. Lett.*, 2005, **87**, 083506.
4 A. J. Moulé and K. Meerholz, *Adv. Funct. Mater.*, 2009, **19**, 3028–3036.
5 A. J. Moulé and K. Meerholz, *Adv. Mater.*, 2008, **20**, 240–245.
6 W. L. Ma, C. Y. Yang, X. Gong, K. Lee and A. J. Heeger, *Adv. Funct. Mater.*, 2005, **15**, 1617–1622.
7 G. Li, R. Zhu and Y. Yang, *Nat. Photonics*, 2012, **6**, 153–161.
8 J. You, L. Dou, K. Yosimura, T. Kato, K. Ohya, T. Moriarty, K. Emery, C.-C. Chen, J. Gao, G. Li and Y. Yang, *Nat. Commun.*, 2013, 1446.
9 A. Baumann, T. J. Savenije, D. H. K. Murthy, M. Heeney, V. Dyakonov and C. Deibel, *Adv. Funct. Mater.*, 2011, **21**, 1687–1692.
10 S. Barrau, V. Andersson, F. Zhang, S. Masich, J. Bijleveld, M. R. Andersson and O. Inganas, *Macromolecules*, 2009, **42**, 4646–4650.

This journal is © The Royal Society of Chemistry 2013

Energy Environ. Sci., 2013, **6**, 3060–3070 | **3069**

11 K. Maturova, S. S. van Bavel, M. M. Wienk, R. A. J. Janssen and M. Kemerink, *Adv. Funct. Mater.*, 2011, **21**, 261–269.

12 R. J. Kline and M. D. McGehee, *Polym. Rev.*, 2006, **46**, 27–45.

13 S. R. Cowan, A. Roy and A. J. Heeger, *Phys. Rev. B: Condens. Matter Mater. Phys.*, 2010, **82**, 245207.

14 V. D. Mihailetchi, H. X. Xie, B. de Boer, L. J. A. Koster and P. W. M. Blom, *Adv. Funct. Mater.*, 2006, **16**, 699–708.

15 B. A. Collins, J. R. Tumbleston and H. Ade, *J. Phys. Chem. Lett.*, 2011, **2**, 3135–3145.

16 D. M. Huang, S. A. Mauger, S. Friedrich, S. J. George, D. Dumitriu-LaGrange, S. Yoon and A. J. Moulé, *Adv. Funct. Mater.*, 2011, **21**, 1657–1665.

17 Y. Zhao, S. Shao, Z. Xie, Y. Geng and L. Wang, *J. Phys. Chem. C*, 2009, **113**, 17235–17239.

18 S. E. Shaheen, C. J. Brabec, N. S. Sariciftci, F. Padinger, T. Fromherz and J. C. Hummelen, *Appl. Phys. Lett.*, 2001, **78**, 841–843.

19 F. Padinger, R. S. Rittberger and N. S. Sariciftci, *Adv. Funct. Mater.*, 2003, **13**, 85–88.

20 Y. Kim, S. Cook, S. M. Tuladhar, S. A. Choulis, J. Nelson, J. R. Durrant, D. D. C. Bradley, M. Giles, I. McCulloch, C. S. Ha and M. Ree, *Nat. Mater.*, 2006, **5**, 197–203.

21 S. Gunes, H. Neugebauer and N. S. Sariciftci, *Chem. Rev.*, 2007, **107**, 1324–1338.

22 D. M. DeLongchamp, R. J. Kline and A. Herzing, *Energy Environ. Sci.*, 2012, **5**, 5980–5993.

23 S. van Bavel, E. Sourty, G. de With, K. Frolic and J. Loos, *Macromolecules*, 2009, **42**, 7396–7403.

24 S. van Bavel, E. Sourty, G. de With, S. Veenstra and J. Loos, *J. Mater. Chem.*, 2009, **19**, 5388–5393.

25 S. S. van Bavel, E. Sourty, G. de With and J. Loos, *Chin. J. Polym. Sci.*, 2009, **27**, 85–92.

26 S. S. van Bavel, E. Sourty, G. de With and J. Loos, *Nano Lett.*, 2009, **9**, 507–513.

27 A. A. Herzing, L. J. Richter and I. M. Anderson, *J. Phys. Chem. C*, 2010, **114**, 17501–17508.

28 M. Pfannmoller, H. Flugge, G. Benner, I. Wacker, C. Sommer, M. Hanselmann, S. Schmale, H. Schmidt, F. A. Hamprecht, T. Rabe, W. Kowalsky and R. R. Schroder, *Nano Lett.*, 2011, **11**, 3099–3107.

29 N. D. Treat, M. A. Brady, G. Smith, M. F. Toney, E. J. Kramer, C. J. Hawker and M. L. Chabinyc, *Adv. Energy Mater.*, 2011, **1**, 82–89.

30 B. A. Collins, E. Gann, L. Guignard, X. He, C. R. McNeill and H. Ade, *J. Phys. Chem. Lett.*, 2010, **1**, 3160–3166.

31 M. A. Ruderer, R. Meier, L. Porcar, R. Cubitt and P. Mueller-Buschbaum, *J. Phys. Chem. Lett.*, 2012, **3**, 683–688.

32 C. Müller, J. Bergqvist, K. Vandewal, K. Tvingstedt, A. S. Anselmo, R. Magnusson, M. I. Alonso, E. Moons, H. Arwin, M. Campoy-Quiles and O. Inganas, *J. Mater. Chem.*, 2011, **21**, 10676–10684.

33 H. Chen, R. Hegde, J. Browning and M. D. Dadmun, *Phys. Chem. Chem. Phys.*, 2012, **14**, 5635–5641.

34 A. Moulé, J. Bonekamp and K. Meerholz, *J. Appl. Phys.*, 2006, **100**, 094503.

35 C. Muller, T. A. M. Ferenczi, M. Campoy-Quiles, J. M. Frost, D. D. C. Bradley, P. Smith, N. Stingelin-Stutzmann and J. Nelson, *Adv. Mater.*, 2008, **20**, 3510.

36 J. Zhao, A. Swinnen, G. Van Assche, J. Manca, D. Vanderzande and B. Van Mele, *J. Phys. Chem. B*, 2009, **113**, 1587–1591.

37 J. D. Roehling, K. J. Batenburg, F. B. Swain, I. Arslan and A. J. Moulé, *Adv. Funct. Mater.*, 2013, **23**, 2115–2122.

38 W. Ma, C. Yang and A. Heeger, *Adv. Mater.*, 2007, **19**, 1387–1390.

39 J. S. Moon, J. K. Lee, S. Cho, J. Byun and A. J. Heeger, *Nano Lett.*, 2009, **9**, 230–234.

40 O. Wodo, S. Tirthapura, S. Chaudhary and B. Ganapathysubramanian, *Org. Electron.*, 2012, **13**, 1105–1113.

41 O. Wodo, S. Tirthapura, S. Chaudhary and B. Ganapathysubramanian, *J. Appl. Phys.*, 2012, **112**, 064316.

42 K. J. Batenburg and J. Sijbers, *IEEE Trans. Image Process.*, 2011, **20**, 2542–2553.

43 S. Bals, K. J. Batenburg, J. Verbeeck, J. Sijbers and G. Van Tendeloo, *Nano Lett.*, 2007, **7**, 3669–3674.

44 K. J. Batenburg, S. Bals, J. Sijbers, C. Kuebel, P. A. Midgley, J. C. Hernandez, U. Kaiser, E. R. Encina, E. A. Coronado and G. Van Tendeloo, *Ultramicroscopy*, 2009, **109**, 730–740.

45 H. W. Ro, B. Akgun, B. T. O'Connor, M. Hammond, R. J. Kline, C. R. Snyder, S. K. Satija, A. L. Ayzner, M. F. Toney, C. L. Soles and D. M. DeLongchamp, *Macromolecules*, 2012, **45**, 6587–6599.

46 J. D. Roehling, C. W. Rochester, H. W. Ro, K. J. Batenburg, P. Wang, I. Arslan, D. Delongchamp and A. J. Moulé, *J. Phys. Chem. C*, 2013, in preparation.

47 S. A. Mauger, L. Chang, S. Friedrich, C. W. Rochester, D. M. Huang, P. Wang and A. Moulé, *Adv. Funct. Mater.*, 2013, **23**, 1935–1946.

48 S. van Bavel and J. Loos, *Adv. Funct. Mater.*, 2010, **20**, 32173234.

49 B. Ganapathysubramanian and N. Zabaras, *Comput. Meth. Appl. Mech. Eng.*, 2008, **197**, 3560–3573.

50 R. B. Ross, C. M. Cardona, F. B. Swain, D. M. Guldi, S. G. Sankaranarayanan, E. Van Keuren, B. C. Holloway and M. Drees, *Adv. Funct. Mater.*, 2009, **19**, 2332–2337.

51 J. D. Roehling, I. Arslan and A. J. Moulé, *J. Mater. Chem.*, 2012, **22**, 2498–2506.

52 A. J. Moulé, S. Allard, N. M. Kronenberg, A. Tsami, U. Scherf and K. Meerholz, *J. Phys. Chem. C*, 2008, **112**, 12583–12589.

53 G. Garcia-Belmonte, *Solid-State Electron.*, 2013, **79**, 201–205.

54 M. A. Alam, B. Ray, M. R. Khan and S. Dongaonkar, *J. Mater. Res.*, 2013, **28**, 541–557.

55 H. Wang, E. Gomez, J. Kim, Z. Guan, C. Jaye, D. Fischer, A. Kahn and Y. Loo, *Chem. Mater.*, 2011, **23**, 2020–2023.

56 W.-R. Wu, U. S. Jeng, C.-J. Su, K.-H. Wei, M.-S. Su, M.-Y. Chiu, C.-Y. Chen, W.-B. Su, C.-H. Su and A.-C. Su, *ACS Nano*, 2011, **5**, 6233–6243.

57 V. D. Mihailetchi, J. Wildeman and P. W. M. Blom, *Phys. Rev. Lett.*, 2005, **94**, 126602.

58 G. Li, Y. Yao, H. Yang, V. Shrotriya, G. Yang and Y. Yang, *Adv. Funct. Mater.*, 2007, **17**, 1636–1644.

3070 | *Energy Environ. Sci.*, 2013, **6**, 3060–3070

This journal is © The Royal Society of Chemistry 2013